Sequential electrocatalytic reactions along a membrane electrode assembly drive efficient nitrate-to-ammonia conversion

Yuan, Tiange; Li, Min; Subramanian, Siddhartha; Kok, Jesse; Li, Mengran; Urakawa, Atsushi; Voznyy, Oleksandr; Burdyny, Thomas

DOI
10.1016/j.xcrp.2024.101977

Publication date
2024

Document Version
Final published version

Published in
Cell Reports Physical Science

Cell Reports
Physical Science

CellPress
OPEN ACCESS

Article

Sequential electrocatalytic reactions along a membrane electrode assembly drive efficient nitrate-to-ammonia conversion

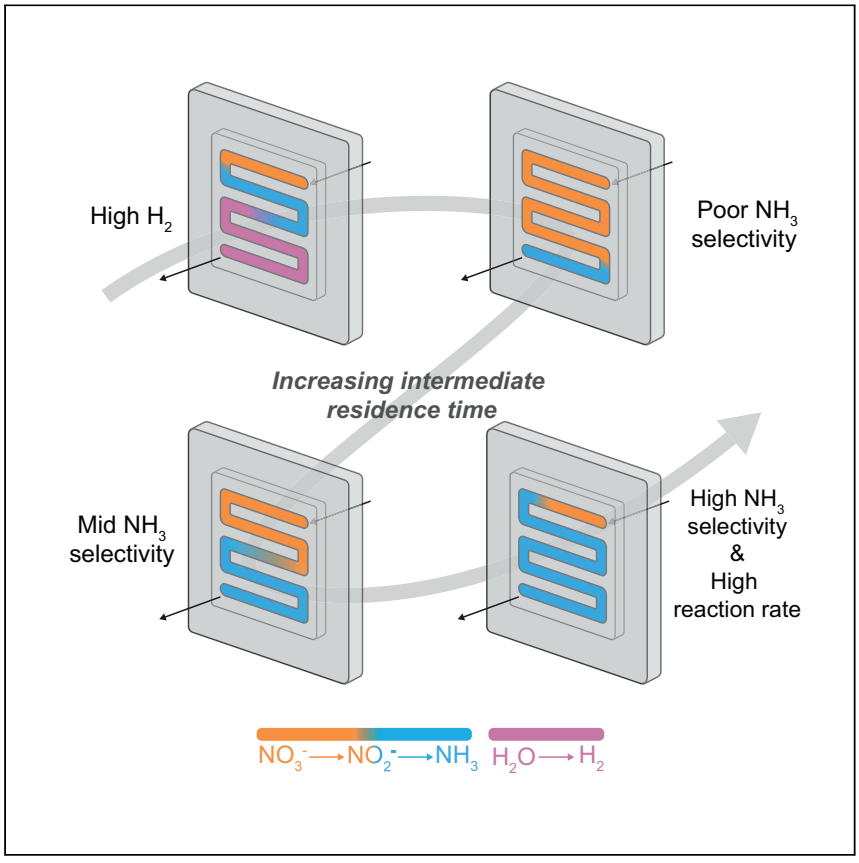

Yuan et al. produce ammonia from nitrate via a two-step sequential reaction in a membrane electrode assembly, utilizing flow rates to control reactivity at elevated current densities. This work shows that controlling the intermediate residence time and traditional engineering principles can substantially boost selectivity, even for simple catalysts.

Tiange Yuan, Min Li, Siddhartha Subramanian, ..., Atsushi Urakawa, Oleksandr Voznyy, Thomas Burdyny

o.voznyy@utoronto.ca (O.V.)
t.e.burdyny@tudelft.nl (T.B.)

Highlights

>90% selectivity and 1.8 A for nitrate reduction to ammonia on unmodified copper catalyst

Membrane electrode assembly overcomes the limitations of a sequential mechanism

Residence time of intermediates determines product selectivity

Intermediate residence time can be tuned by altering system operation parameters

Yuan et al., Cell Reports Physical Science 5, 101977
June 19, 2024
https://doi.org/10.1016/j.xcrp.2024.101977

Cell Reports
Physical Science

CellPress
OPEN ACCESS

Article

Sequential electrocatalytic reactions along a membrane electrode assembly drive efficient nitrate-to-ammonia conversion

Tiange Yuan,[1,2,4] Min Li,[1] Siddhartha Subramanian,[1] Jesse Kok,[1] Mengran Li,[1,3] Atsushi Urakawa,[1] Oleksandr Voznyy,[2,*] and Thomas Burdyny[1,5,*]

SUMMARY

Electrochemical ammonia (NH_3) synthesis from nitrate (NO_3^-) offers a promising greener alternative to the fossil-fuel-based Haber-Bosch process to support the increasing demand for nitrogen fertilizers while removing environmental waste. Previous studies have mainly focused on designing catalysts to promote the direct conversion ($NO_3^- \rightarrow NH_3$) while suppressing the two-step pathway ($NO_3^- \rightarrow NO_2^- \rightarrow NH_3$). We hypothesize that efficient nitrate reduction is possible on simple catalysts by instead promoting the two-step reaction and using chemical reactor principles in a membrane electrode assembly, despite NO_2^- intermediates. Here, we use an unmodified copper catalyst and control reactivity through current density, flow rate, and electrolyte recycling. Balancing the electrolyte flow rate with current density results in ideal residence times for NO_2^-, allowing for 91% FE_{NH3} in a 5 cm^2 electrolyzer with a NO_3^- to NH_3 partial current of 1.8 A. This work shows that traditional engineering principles can substantially boost the NO_3 reduction reaction, even for simple catalysts.

INTRODUCTION

Current nitrogen fertilizer production is highly fossil fuel based, leading to considerable CO_2 emissions. The Haber-Bosch process converts nitrogen gas (N_2) with hydrogen (H_2) (derived from natural gas) to ammonia (NH_3) under high temperatures and high pressures (Figure 1A). Approximately 2% of global energy consumption and 40 Mt of CO_2 emissions are associated with nitrogen fertilizer production annually.[1] Additionally, large-scale Haber-Bosch facilities centralize production to lower costs, leading to increased energy consumption from transportation to the decentralized end-use locations. Thus, there is an urgent need to develop sustainable ammonia production routes using renewable energy sources as the input. As a result, electrochemical ammonia synthesis routes have gained attention.

Multiple approaches have been developed for the electrochemical reduction of N_2 (N_2 reduction reaction [NRR]), including an NRR in the aqueous system[2–9] and lithium-mediated N_2 reduction in the organic solution (Li-NRR).[10–16] At present, the aqueous NRR suffers from the inert nature of N_2 and is being kinetically outcompeted by the hydrogen evolution reaction (HER).[8,17] Although different strategies have been applied to break scaling relationships between the NRR and the HER, the current aqueous performance is still limited at ~10 mA cm^{-2}. Additionally, the low yield of NRR and improper experimental protocols have led to numerous false positives due to contamination.[7,18–21] On the other hand, Li-NRR utilizes the highly

[1]Department of Chemical Engineering, Delft University of Technology, Van der Maasweg 9, 2629 HZ Delft, the Netherlands

[2]Department of Physical and Environmental Sciences, University of Toronto, 1265 Military Trail, Toronto, ON M1C 1A4, Canada

[3]Department of Chemical Engineering, The University of Melbourne, Parkville, VIC, Australia

[4]X (formerly Twitter): @tiange_yuan

[5]Lead contact

*Correspondence: o.voznyy@utoronto.ca (O.V.), t.e.burdyny@tudelft.nl (T.B.)

https://doi.org/10.1016/j.xcrp.2024.101977

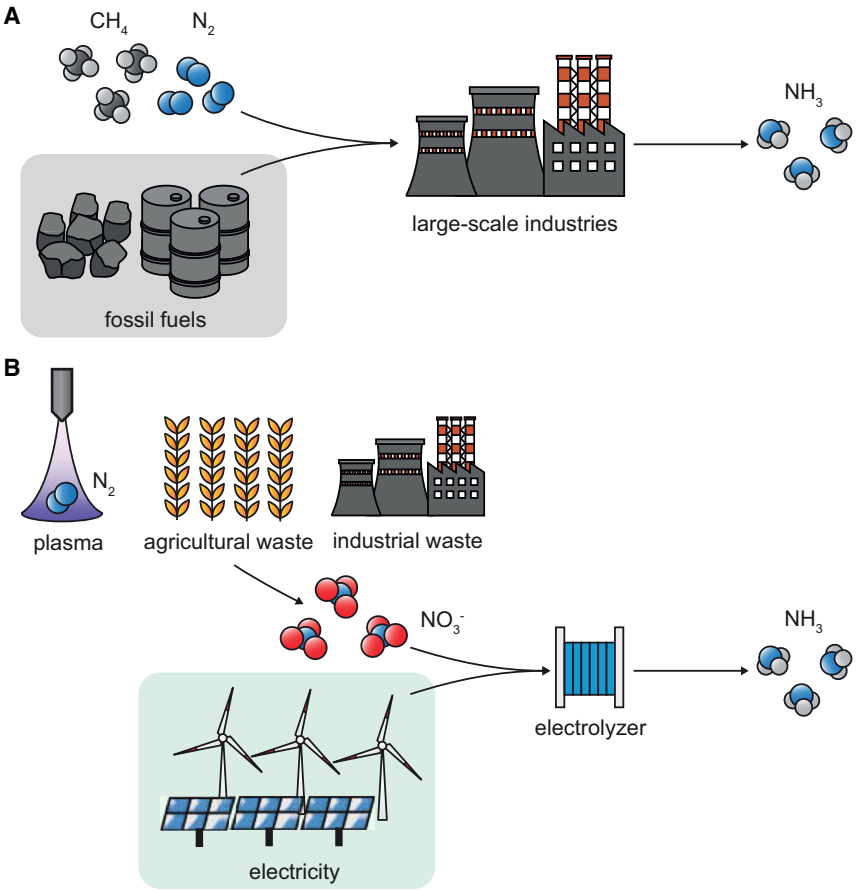

Figure 1. Comparison between traditional ammonia production and the proposed electrochemical alternative

(A) Current Haber-Bosch process for ammonia production, which requires N_2 and CH_4 as starting materials and fossil fuels as the energy source.

(B) Proposed electrochemical-based ammonia production with NO_3^- as the reactant and renewable electricity as the energy source.

active lithium metal to react with N_2. Li^+ is electrochemically reduced into metallic lithium metal, which later forms Li_3N upon contact with N_2. Li_3N then reacts with proton sources to form NH_3 and Li^+. The Li-NRR can achieve nearly 100% Faradaic efficiency (FE) to ammonia at industrial-relevant current densities.[16] However, high full-cell voltages associated with the Li-NRR lead to high energy consumption.[14]

Nitrate (NO_3^-) can be an alternative nitrogen source for fertilizer synthesis. NO_3^- is more reactive than N_2 and is considered a environmental pollutant, giving its removal an added benefit[22,23] (Figure 1B). Wastewater from agriculture, explosives factories, and mine industries contain a considerable amount of NO_3^-, especially nuclear wastewater.[22] The presence of NO_3^- in water causes eutrophication in aqueous ecosystems and threatens drinking water safety. Thus, removing NO_3^- from water using electricity is an attractive approach for waste remediation, particularly if it can also be converted into a valuable compound and complete the nitrogen cycle. Previous studies have investigated the electrochemical reduction of NO_3^- into N_2,[24,25] but the direct electrochemical NO_3^- conversion to NH_3 (NO_3RR) has gained more traction in recent years.[24,26–35] A few studies have discussed the unique potential of the NO_3RR in future sustainable development.[22,23,36] We take the view that electrochemical N_2 reduction to NH_3 and

electrochemical NO_3^- conversion to NH_3 are two very different reactions and fields of interest. For ammonia production, these two fields have different markets and targets. NRRs (both aqueous and Li-mediated) would act as a competitor to the current Haber-Bosch process. Li-NRR systems have substantial equilibrium cell voltages (>3 V), which makes them fundamentally tough to compete against renewable H_2 + Haber-Bosch. Conversely, the NO_3RR requires lower energy to perform. In our view, the NO_3RR has the potential now as a waste stream mediator and efficient ammonia production route, albeit at smaller maximum market sizes than potential NRRs.

Numerous previous studies have reported NO_3RRs in the laboratory-scale batch reactor—typically called an H-cell. On many electrocatalytic surfaces, however, NO_3^- can be reduced to either nitrite (NO_2^-) or NH_3 ($NO_3^- \rightarrow NH_3$). Additionally, NO_2^- can act as an intermediate for ammonia production such that a two-step reaction occurs ($NO_3^- \rightarrow NO_2^- \rightarrow NH_3$). In batch reactor experiments, however, where the reactant concentration of a well-mixed vessel becomes homogeneous, it is important to catalytically maximize the single-step reaction $NO_3^- \rightarrow NH_3$ to reach a high FE and current densities (j) toward NH_3. Otherwise, NO_2^- that is produced at the electrode will diffuse back into the bulk electrolyte, leading to a lower selectivity toward NH_3. As a result, many efforts have gone into tuning catalyst compositions and structures to suppress NO_2^- formation through bimetallic[26,33] or single-atom catalysts.[27,30] Other works have used a catalytic tandem approach to reduce by-product NO_2^- before it can diffuse back into the bulk electrolyte.[32,37]

Although great efforts have been put into designing catalysts for the batch reactor environment, comparatively few studies[38–40] have utilized more compact membrane electrode assembly (MEA) configurations that, in the future, are needed to lower cell internal resistance and provide better scalability potential.[41] Other fields in electrolysis[42] have pointed out that (1) knowledge learned from H-cells is not fully transferable to MEAs and (2) catalysts' performances can differ dramatically from H-cell to MEA, especially in product selectivity. Aside from the efficiency and volume benefits of an MEA electrolyzer, the system allows for reagents to flow past the electrodes (Figure 2B) in a much more controlled environment than H-cells. Control over the reagent, by-product, and product concentrations is then much greater and can provide unexplored utility for NO_3RRs by varying operation conditions such as flow rates, flow patterns, and operating modes (circulation vs. single pass).

In this work, we hypothesized that the use of an MEA could overcome the limitations of a sequential reaction mechanism ($NO_3^- \rightarrow NO_2^- \rightarrow NH_3$ in Figure 2C) for NO_3RRs, providing less emphasis on catalyst design and aiding in the faster applicability of the technology. After assembling an MEA system for the NO_3RR, we then explored how operating parameters impact measured nitrite and ammonia FEs for various flow rates and current densities. We found that by taking advantage of the residence time of by-product NO_2^-, we achieved near-unity ammonia FEs at current densities of 395 mA/cm^2. Our findings suggest that the catholyte flow rate impacts the residence time of reactants/intermediates which alters product selectivity. We further examined the trade-offs between NO_3^- full conversion and FE_{NH3} by comparing recirculating vs. single-pass operations.

RESULTS

Electrolyzer setup

To explore the sequential NO_3^- conversion in an MEA, the copper catalyst was tested in an MEA with a 5 cm^2 active area.[43] Copper was sputtered on a carbon

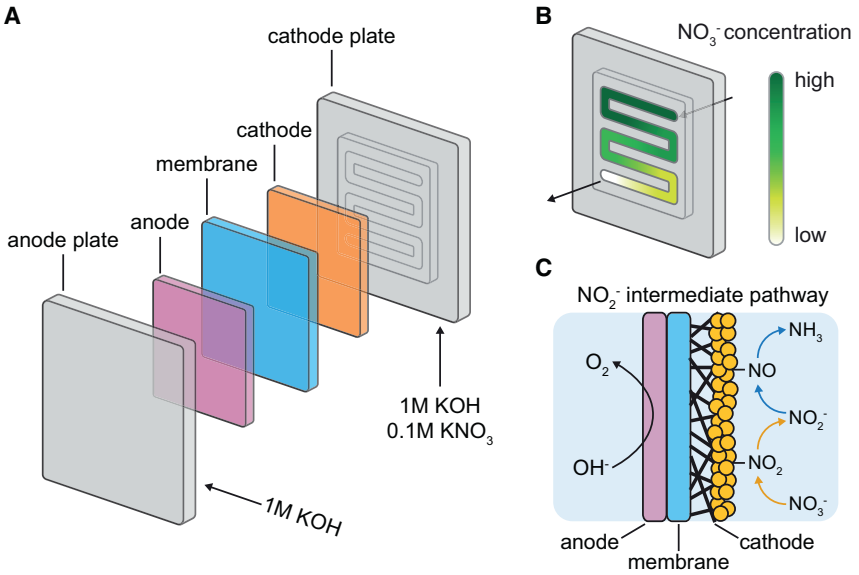

Figure 2. Schematics of our MEA setup, key characteristics, and key reactions

(A) The structure of our MEA includes copper on carbon paper as the cathode, a membrane, and a nickel foam as the anode.

(B) NO_3^- concentration gradient along the flow field in the MEA.

(C) NO_3^- conversion to NH_3 via the two-step sequential pathway.

substrate (Figure S1) as the working electrode with 1 M KOH + 0.1 M KNO_3 as the catholyte (Figure 2A). A hydrophilic macropore carbon paper was chosen as the substrate to promote mass transport from the aqueous to the electrode.[44] We explored the effect of the catalyst-facing direction, and these data are shown in Figure S4. When copper was placed toward the membrane instead of toward the flow field, the total FE toward NO_3^- conversion (FE_{NH3}+FE_{NO2-}) decreased. These results indicate that NO_3^- diffusion through the carbon support was limited, resulting in a higher HER when the operating current density is fixed at rates beyond NO_3^- transport. Based on catalyst orientation results, the copper catalyst was placed toward the flow field to reduce the distance between the bulk catholyte nitrate and the copper layer. A nickel foam was used as the counter electrode with 1 M KOH as the anolyte. A cation exchange membrane separated the two electrodes. Detailed experimental procedures can be found in the experimental procedures, and pictures of each cell part can be found in Figure S2.

Analyzing the effects of NO_3^- residence time on the dominant product formed

At a fixed current density, the location and reactions occurring can be influenced by controlling the flow rate of NO_3^- through the MEA cell (Figure 3A). With a high concentration of NO_3^-, $NO_3^- \rightarrow NO_2^-$ (Figure 3B) should be the dominant reaction near the inlet, and a concentration gradient of NO_3^- along the flow field should occur (Figure 2B). As NO_3^- is converted to NO_2^- on copper, the concentration of NO_2^- should reach a maximum at a certain point in the flow channel, and the dominant reaction will switch to $NO_2^- \rightarrow NH_3$ (colored in blue in Figure 3B). When NO_2^- is fully depleted near the electrode surface, the HER will take over (colored in pink in Figure 3B).

We hypothesized that catholyte flow rates determine the residence time of reactants with a negative correlation, further impacting product distributions. With low flow rates, long NO_3^- residence times should lead to fast NO_3^- depletion with fast

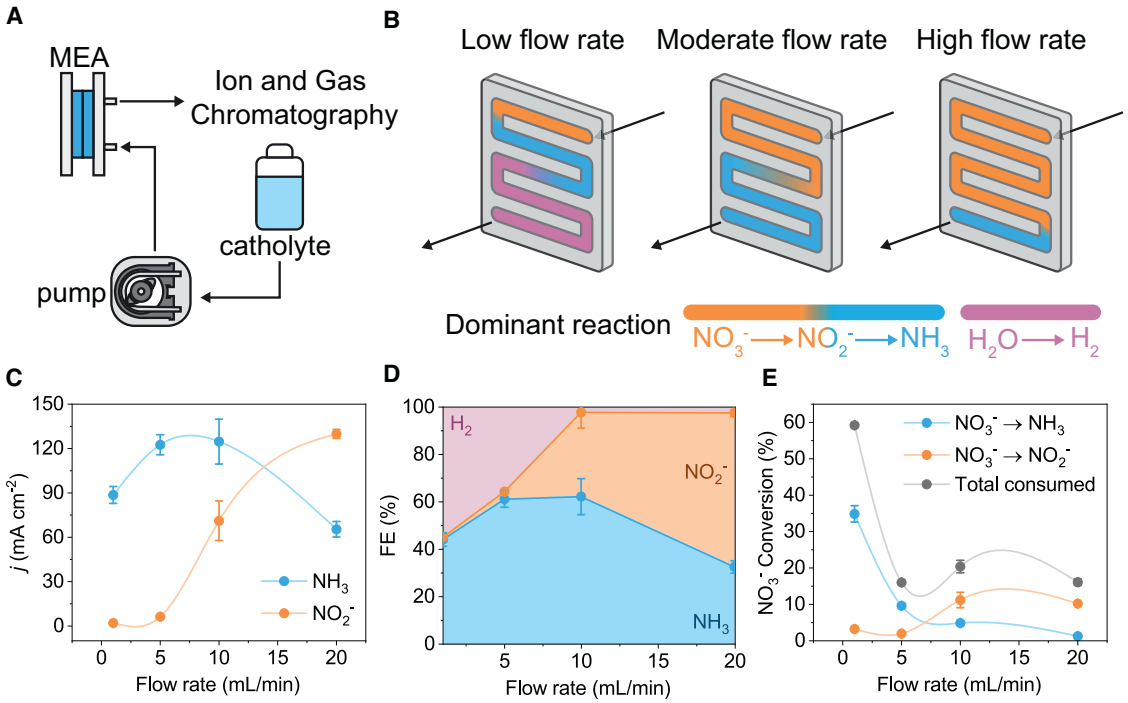

Figure 3. Single-pass experiments at 200 mA cm^{-2} with different catholyte flow rates

(A) Schematic of catholyte single-pass experiment with 1 M KOH + 0.1 M KNO_3 as catholyte.

(B) Schematic of hypothesized dominant reactions along the flow channel.

(C) Partial current densities of NO_2^- and NH_3.

(D) Faradaic efficiency of NH_3, NO_2^-, and H_2 where area represents FE.

(E) Conversion of NO_3^-, NO_3^- to NO_2^-, and NO_3^- to NH_3.

Error bars represent the standard deviation from three replicates.

NO_2^- accumulation (Figure 3B, first image). The dominant reaction is expected to switch from NO_3^- → NO_2^- to NO_2^- → NH_3 close to the inlet. Once NO_2^- is fully consumed, the HER should dominate the flow channel near the outlet. Thus, H_2 and NH_3 are expected as major products at low catholyte flow rates. At moderate flow rates, the dominant reaction should switch from NO_3^- → NO_2^- to NO_2^- → NH_3 further away from the inlet since the residence time of NO_3^- is shortened (Figure 3B, second image). NO_2^- → NH_3 should dominate the second half of the cell with a minimum HER. NH_3 and leftover NO_2^- are expected to be major products. At high flow rates, the switch from NO_3^- → NO_2^- to NO_2^- → NH_3 should occur near the outlet due to a short NO_3^- residence time (Figure 3B, third image). A large portion of NO_2^- should remain unreacted and escape from the outlet. High NO_2^-/NH_3 ratios are expected with high flow rates.

Single-pass experiments were carried out to verify our hypothesis. One advantage of single-pass operation is the consistency of catholyte composition over time. We fixed the current density at −200 mA cm^{-2} and tested catholyte flow rates at 1, 5, 10, and 20 mL/min. Products were analyzed by ion chromatography (IC) and gas chromatography (GC). The flow diagram of the single-pass experiment can be found in Figure S3.

Product selectivity results align with our hypothesis across different flow rates in Figure 3D. At low flow rates (1 and 5 mL/min), NH_3 was the dominant nitrogen product (44.3% and 61.3% FE_{NH3}) with nearly zero FE_{NO2-} (1.0% and 3.2%), while HER was

the major side reaction (Figure S5). At moderate (10 mL/min) and high (20 mL/min) flow rates, HER was suppressed to nearly zero (Figure S5). FE_{NO2-} increased to 65.0% with 20 mL/min, while FE_{NH3} dropped to 32.7%. To better compare the selectivity of NH_3 over NO_2^-, we calculated the ratio between FE_{NH3} and FE_{NO2-} (FE_{NH3}/FE_{NO2-}) and observed a negative correlation with flow rates (Figure S6). Nitrogen mass balance was calculated to further verify the FE results (Figure S7). We found 20% of nitrogen was missing at 1 mL/min. At 1 mL/min, a high NH_3 concentration accumulated during the reaction in the catholyte (>600 ppm) could lead to high diffusion from the catholyte to the anolyte or high volatilization into the air. Since NO_3^-, NO_2^-, and NH_3 were not observed in the anolyte, we suspect that the counter electrode could also oxidize NH_3 to gas products (e.g., N_2). Under a fixed current density, partial current densities (Figure 3C) followed the same trend as FE, with the highest $j_{NH3} = -125$ mA cm^{-2} at 10 mL/min and the highest $j_{NO2-} = -130$ mA cm^{-2} at 20 mL/min. The maximum yield of NH_3 was 10,492 μg h^{-1} cm^{-2}, and the yield of NO_2^- was 111,524 μg h^{-1} cm^{-2}, as shown in Figure S8. The total conversion rate was 59% with the lowest flow rate (Figure 3E) and fell below 20% with moderate and high flow rates.

We excluded ^{15}N experiments from our study due to the following reasons: (1) we obtained >1,000 ppm synthesized NH_3 in the electrolyte with most conditions, which is much higher compared to potential ambient containment levels; (2) nitrogen mass balance (including leftover NO_3^-, NO_2^-, NH_3) after the electrochemical reaction showed that the total measured N content at the outlet of the reactor summed to nearly 100% (generated NH_3 + NO_2^- + leftover NO_3^- vs. inputted NO_3^-) (Figure S7); and (3) a recent study[36] points out the unnecessity of ^{15}N experiments in NO_x electrochemical reduction to NH_3 studies, which aligns with our thoughts. Thus, ^{15}N isotope experiments were excluded in our study.

The full-cell potential in an MEA is a combination of cathode overpotential, anode overpotential, membrane resistance, interface resistance, Nernstian pH losses, and thermodynamic potential, plus other losses. For our flow rate study with a constant current density, we assume that the cathode overpotential dominantly affects the full-cell potential. Full-cell voltages were −2.8 V at 1 mL/min (Figure S9), which could be due to the high HER, while with 20 mL/min, the full-cell voltages decreased to −2.4 V with no HER.

We conducted two sets of control experiments to further prove our hypothesis. The catalytic activity of our bare carbon support (Figure S10) was examined. Bare carbon paper exhibited low FE_{NO2-} even with high catholyte flow rates. The results on bare carbon paper show that (1) sputtered copper is capable of promoting sequential NO_3^- conversion to NH_3 via NO_2^- and (2) material with a single-step NO_3RR reaction pathway is not affected by high flow rates due to the lack of an intermediate—NO_2^-. We then conducted NO_2^- electrochemical reduction with different flow rates as additional control experiments (Figure S17). We observed ∼45% FE_{NH3} at 1 mL/min, while FE_{NH3} remained at ∼76% for 5–20 mL/min. Results at 1 mL/min indicate a NO_2^- mass transport limitation triggering a high HER. Catholyte flow rates beyond 5 mL/min can mitigate the reactant mass transport limitation. NO_2^- conversion results further confirm that the selectivity of a one-step reaction ($NO_2^- \rightarrow NH_3$) is unaffected by high flow rates.

From the flow rate study, low flow rates led to a high single-pass conversion of nitrate, but considerably more unwanted HERs occurred as a result. These higher HER rates also increased the full-cell voltage. Although high flow rates resulted in

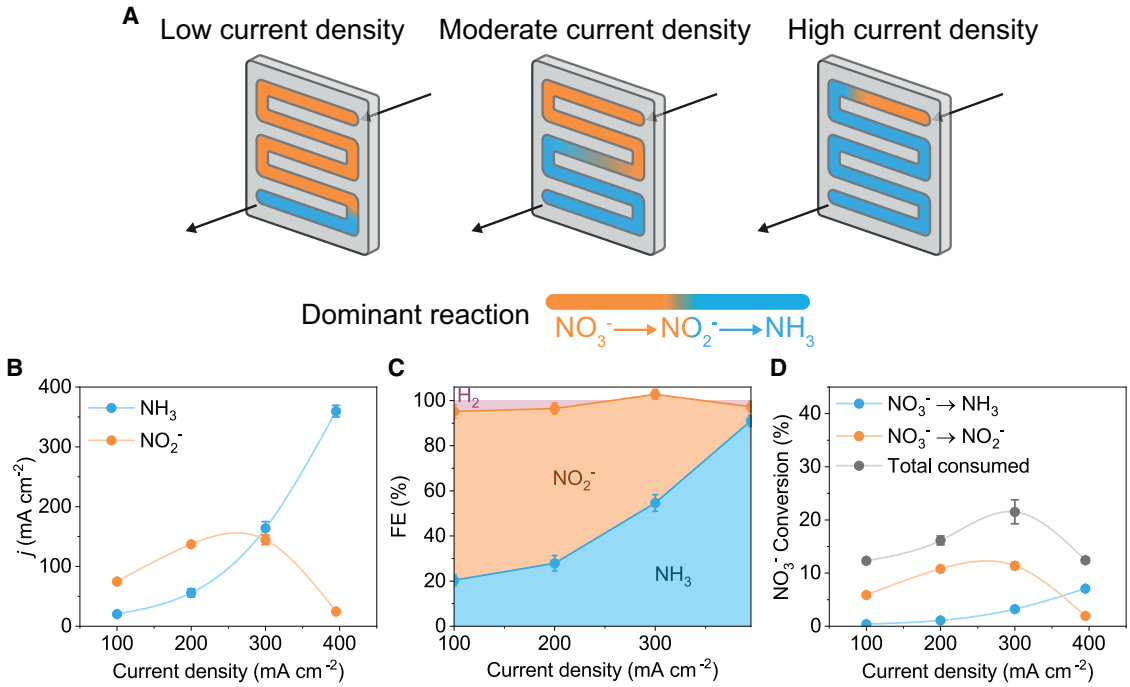

Figure 4. Single-pass experiments at a 20 mL/min catholyte flow rate with different current densities

(A) Schematic of hypothesized dominant reactions along the flow channel.

(B) Partial current densities of NO_2^- and NH_3.

(C) Faradaic efficiency of NH_3, NO_2^-, and H_2 where area represents FE.

(D) Conversion of NO_3^-, $NO_3^- \rightarrow NO_2^-$, and $NO_3^- \rightarrow NH_3$.

Error bars represent the standard deviation from three replicates.

low single-pass conversion and low selectivity of NH_3 over NO_2^-, FE_{NO2-}+FE_{NH3} was almost 100% with lower full-cell voltages at high flow rates, meaning that HERs can be avoided. In the next two sections, we explored two strategies possible with the MEA cell to boost the performance metrics of ammonia production: (1) boosting FE_{NH3} over FE_{NO2-} using a mixture of high flow rates and varying current densities and (2) increasing the overall NO_3^- conversion rates via recirculation while maintaining high NH_3 FEs.

Maximizing ammonia production by tailoring current densities with flow rates

Our single-pass experiments at -200 mA cm^{-2} with 20 mL/min in Figure 3 suggest that a short residence time leads to high leftover NO_2^- and that the electron supply rate at -200 mA cm^{-2} is not fast enough to consume the remaining NO_2^-. We then hypothesized that in the MEA, we could maintain high flow rates to limit HER formation while increasing the operating current density to convert excess NO_2^- into NH_3. Thus, at 20 mL/min, higher current densities should favor FE_{NH3} over FE_{NO2-}, while lower current densities should further promote FE_{NO2-} (Figure 4A). We then conducted further single-pass experiments with a fixed 20 mL/min catholyte flow rate and varied the current densities from -100 to -395 mA cm^{-2}.

The total FE toward NO_2^- and NH_3 remained at nearly 100% with <5% FE for gas products even at -395 mA cm^{-2}, highlighting that we can limit HER formation (Figure 4C). At 20 mL/min, FE_{NO2-} descended to 6% with higher current densities, while FE_{NH3} increased and peaked at 91% at -395 mA cm^{-2}. Full-cell voltage increased linearly with increasing current densities and reached -3.5 V at -395 mA cm^{-2}

(Figure S14), which indicates substantial cell voltage from ohmic/membrane resistances. High full-cell voltages at high current densities can be reduced in the future through proper MEA design and increasing anolyte concentrations.

The highest yield of NH_3 was 30,262 μg h^{-1} cm^{-2} (Figure S11). The ratio of FE_{NH3}/FE_{NO2-} showed a positive relationship with current densities at 20 mL/min (Figure S12). The partial current density for NH_3 showed a non-linear relationship from −20 to −360 mA cm^{-2} (Figure 4B). Combined, these results indicate that current density can be matched with flow rate to achieve high NH_3 FEs. While we could not test higher current densities due to the amperage limit of our potentiostat, we anticipate that further elevated current densities could also be achieved with higher inlet flow rates.

For nitrate conversion rates (Figure 4D), we calculated conversion percentages based on NH_3 concentrations, NO_2^- concentrations, and final NO_3^- concentrations (to calculate the total consumed in Figure 4D). However, it should be pointed out that the highest FE_{NH3} and j_{NH3} at −395 mA cm^{-2} did not lead to the highest NO_3^- conversion. The reason is that the $NO_3^- \rightarrow NO_2^- \rightarrow NH_3$ reaction consumes 8 electrons, while $NO_3^- \rightarrow NO_2^-$ is a two-electron process. Moles of NO_3^- consumed can be calculated as follows:

$$\text{moles of } NO_3^- \text{ consumed} = \frac{\text{total charge}}{\text{Faraday constant}}\left(\frac{FE_{NH_3}}{8} + \frac{FE_{NO2}}{2}\right).$$

Thus, under the same current density and time, high FE_{NH3} results in fewer moles of NO_3^- being consumed compared to high FE_{NO2-}. Nitrogen balances were calculated to verify the FE results (Figure S13), and nearly 100% of total nitrogen species were measured.

Full NO_3^- conversion via a circulation operation

In Figure 4, we demonstrated that the sequential NO_3^- conversion to NH_3 is capable of achieving high FEs and current densities for ammonia through proper systematic engineering. Despite the well-controlled nature of the single-pass experiments, a key drawback of single-pass operation is the low conversion rate (<20%) at a high catholyte flow rate setting. In the next section, we explored full NO_3^- conversion through a circulation operation. To tackle the low conversion rate associated with high flow rates, we hypothesized that catholyte circulation could lead to full consumption of NO_3^- but might suffer from high HERs over time. We examined the circulation mode at −200 mA cm^{-2} with a 50 mL catholyte circulated at 20 mL/min (Figure 5A). Liquid samples were extracted from the electrolyte reservoir every 5–10 min.

The concentration profile followed a typical sequential reaction profile (Figure 5B). NO_3^- was fully converted at 50 min via circulation mode (Figure S15B). $NO_3^- \rightarrow NO_2^-$ was the dominant reaction within 0–20 min, where FE_{NO2-} was higher than FE_{NH3} (Figure 5C). NO_2^- as the intermediate was initially accumulated to reach a maximum concentration at 20 min and then was fully consumed (Figure 5B). The NH_3 concentration profile experienced three stages, which can be identified by the slope in Figure 5B. From 0 to 20 min, the NH_3 concentration increased with a small slope due to a lack of NO_2^- in the reservoir. As NO_2^- was accumulated to the maximum at 20 min, the NH_3 concentration started to increase more rapidly from 20 to 60 min. The NH_3 concentration reached a maximum after 60 min, when NO_2^- and NO_3^- were both fully depleted. In the circulation study, we used averaged FE to evaluate the selectivity. Averaged FE_{NH3} begined with 20% at 5 min and reached the highest at 60% from 40 to 60 min (Figure 5C). Averaged FE_{NH3}

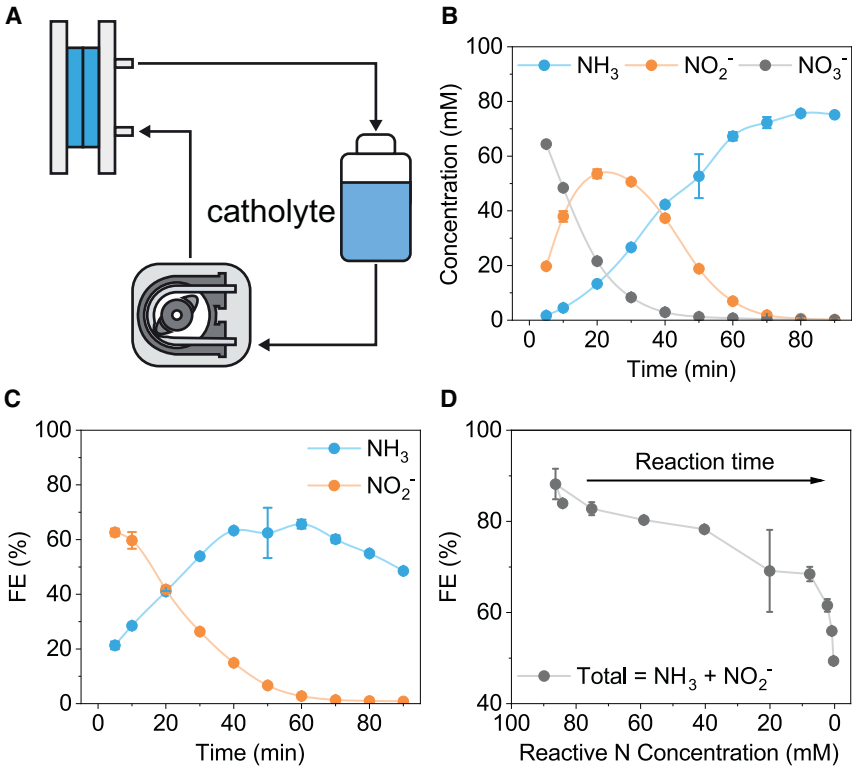

Figure 5. Circulation experiments result with 20 mL/min catholyte flow rate at −200 mA cm^{-2}

(A) Schematic of circulation experiment where 50 mL catholyte was circulated at 20 mL/min.

(B) Concentration of remaining NO_3^-, synthesized NO_2^-, and synthesized NH_3 in catholyte reservoir over time.

(C) Averaged FE_{NH3} and FE_{NO2-} over time.

(D) Total liquid products' FE (FE_{NH3} + FE_{NO2-}) variations with reactive N concentrations ($concentration_{NO3-}$ + $concentration_{NO2-}$).

Error bars represent the standard deviation from three replicates.

started to drop after 60 min and as the HER dominated. The decrease in liquid FEs could be due to the mass transport limitation with the lack of reactive N compounds (NO_3^- and NO_2^-) (Figure 5D). The full-cell voltage was over −3 V when the HER was triggered (Figure S15A), which acts as an additional measure of how the reaction is proceeding.

For nitrogen balance, 90% of nitrogen was measured initially, while ~20% of nitrogen was missing by the end of the circulation experiment. The total missing nitrogen could be attributed to reasons similar to those in the 1 mL/min single-pass experiments (Figure S7) since the concentration of NH_3 reached >1,000 ppm. We also tested the circulation mode at higher current densities, and similar trends were observed in the concentration profile and FE (Figure S16). In short, we demonstrated that electrolyte recirculation can achieve full NO_3^- conversion but suffers from high HERs as NO_3^- and NO_2^- are consumed. Despite our promising results, future work is required to develop strategies to achieve continuous full NO_3^- conversion while maintaining high FE_{NH3}.

DISCUSSION

Our study explored the sequential NO_3^- reduction mechanism in an MEA. Through single-pass experiments, we identified that the residence time of reactants

determines the product selectivity and can be controlled by altering catholyte flow rates. Low flow rates offered high conversion and favored NH_3 over NO_2^- but resulted in high HERs and nitrogen loss. High catholyte flow rates led to high FE_{NH3} + FE_{NO2-} and low HERs but were associated with low conversion rates and low FE_{NH3}/FE_{NO2-} ratios.

Copper has been previously considered a poorly performing catalyst due to its two-step sequential reaction mechanism for the NO_3RR,[23,26,28,32,33,45] but we have seen near-unity ammonia FEs and current densities of 395 mA/cm^2 with this simple catalyst. By balancing between the NO_2^- pool and electron supply rate, we significantly boosted the FE_{NH3}/FE_{NO2-} ratio from 0.3 to 14.6 without any modification on the catalyst. Additionally, we demonstrated full NO_3^- conversion with a circulation mode and pointed out limitations such as mass transport as NO_3^- depleted over time and low average FE_{NH3}. Further advancements in the field can now proceed through these routes.

Our investigation has shown that a two-step sequential NO_3^- reduction catalyst can benefit from the complexity of an MEA and can perform at industrial-relevant current densities. Our study represents a comprehensive examination of MEA operation parameters for sequential NO_3^- conversion. We suggest that NO_3RR design principles learned from H-cells might require tailoring when transferred into the MEA system. Designing NO_3RR catalysts in an MEA could benefit from different criteria compared to those in H-cells. For example, a segmented tandem design along the flow field could be further explored, where a $NO_3^- \rightarrow NO_2^-$ catalyst is fabricated near the inlet and another $NO_2^- \rightarrow NH_3$ catalyst is located at the second half of the flow field. The insights gained from this study offer guidance when transferring previous H-cell-tested catalysts into MEA systems. In our study, we demonstrate the importance of the concentration gradient, mass transport, and residence time. We advocate that future studies should focus on transport modeling to elucidate the magnitude and potential of these parameters to alter performance, similar to efforts performed in electrochemical CO_2 conversion on gas diffusion electrodes.[42,46]

EXPERIMENTAL PROCEDURES

Resource availability

Lead contact

Further information and requests for resources and reagents should be directed to and will be fulfilled by the lead contact, Thomas Burdyny (t.e.burdyny@tudelft.nl).

Materials availability

This study did not generate new unique materials.

Data and code availability

The data presented in this work are available from the corresponding author upon reasonable request.

Materials

Cathodes were prepared through direct-current magnetron sputtering copper (Cu) at a pressure of 3 μbar onto a carbon gas diffusion layer (Sigracet 39 AA, Fuel Cell Store). The thickness of the Cu layer was controlled by adjusting the power supply and sputtering time. Prepared cathodes were stored in a glovebox with an inert atmosphere to minimize oxidation. The cell structure illustration is presented in Figure 2A. Nickel foam (Recemat BV) was used as the anode. Nafion 115 (Ion Power) was pretreated in 1 M KOH prior to experiments and used as the cation exchange

membrane. A 5.06 cm^2 (2.25 × 2.25 cm) electrolyzer was used in this study, where flow fields for the cathode and the anode are serpentine type and pin type, respectively. 1 M KOH + 0.1 M KNO_3 was prepared (KNO_3 99% Alfa Aesar) and used as the catholyte. 1 M KOH was used as the anolyte.

Methods

Flow rates of catholyte and anolyte were controlled by two separate peristaltic pumps (Figure S3). It should be noted that the anolyte was circulated for all experiments. For our two-electrode MEA, the current input was controlled by an electrochemical testing station, and the cell voltage was measured as the response. Cathode liquid samples were collected using a syringe and analyzed by two separate ICs (one for measuring NO_2^- and NO_3^- and one for measuring NH_4^+) (Metrohm). Argon was purged into catholyte headspace, and gas samples were measured by an auto-GC (Global Analyser Solutions).

SUPPLEMENTAL INFORMATION

Supplemental information can be found online at https://doi.org/10.1016/j.xcrp.2024.101977.

ACKNOWLEDGMENTS

The authors acknowledge funding from a Natural Sciences and Engineering Research Council Discovery Grant (2019-04897), the Canada Foundation for Innovation John R. Evans Leaders Fund (project 38101), the Mitacs Globalink Research Award (IT32560), the University of Toronto Scarborough International Research Fund, and the Australian Research Council (DE230100637).

AUTHOR CONTRIBUTIONS

T.Y. and T.B. conceived the project. T.Y. led experiments, data analysis, and figure design. Min Li assisted with electrochemical testing, IC measurements, and scientific discussion. S.S. and J.K. performed catalyst fabrication and assisted with GC measurements. Mengran Li assisted with electrochemical testing, data analysis, and scientific discussion. A.U. assisted with scientific discussion and equipment. O.V. and T.B. assisted with project supervision, scientific discussion, and funding. T.Y. and T.B. wrote the manuscript with editing contributions from all the authors.

DECLARATION OF INTERESTS

The authors declare no competing interests.

Received: December 20, 2023
Revised: February 26, 2024
Accepted: April 19, 2024
Published: May 13, 2024

REFERENCES

1. Giddey, S., Badwal, S.P.S., and Kulkarni, A. (2013). Review of electrochemical ammonia production technologies and materials. Int. J. Hydrogen Energy *38*, 14576–14594. https://doi.org/10.1016/j.ijhydene.2013.09.054.

2. Hao, Y.-C., Guo, Y., Chen, L.-W., Shu, M., Wang, X.-Y., Bu, T.-A., Gao, W.-Y., Zhang, N., Su, X., Feng, X., et al. (2019). Promoting nitrogen electroreduction to ammonia with bismuth nanocrystals and potassium cations in water. Nat. Catal. *2*, 448–456. https://doi.org/10.1038/s41929-019-0241-7.

3. Hao, Z., Yuan, T., Dong, Q., Singh, K., Dinic, F., Zou, Y., Niu, J., and Voznyy, O. (2021). Underappreciated Role of Low-Energy Facets in Nitrogen Electroreduction. ACS Mater. Lett. *3*, 327–330. https://doi.org/10.1021/acsmaterialslett.0c00611.

4. Hu, L., Xing, Z., and Feng, X. (2020). Understanding the Electrocatalytic Interface for Ambient Ammonia Synthesis. ACS Energy Lett. *5*, 430–436. https://doi.org/10.1021/acsenergylett.9b02679.

5. Wang, M., Liu, S., Qian, T., Liu, J., Zhou, J., Ji, H., Xiong, J., Zhong, J., and Yan, C. (2019). Over 56.55% Faradaic efficiency of ambient ammonia synthesis enabled by positively shifting the reaction potential. Nat. Commun.

10, 341. https://doi.org/10.1038/s41467-018-08120-x.

6. Qiu, W., Xie, X.-Y., Qiu, J., Fang, W.-H., Liang, R., Ren, X., Ji, X., Cui, G., Asiri, A.M., Cui, G., et al. (2018). High-performance artificial nitrogen fixation at ambient conditions using a metal-free electrocatalyst. Nat. Commun. *9*, 3485. https://doi.org/10.1038/s41467-018-05758-5.

7. Andersen, S.Z., Čolić, V., Yang, S., Schwalbe, J.A., Nielander, A.C., McEnaney, J.M., Enemark-Rasmussen, K., Baker, J.G., Singh, A.R., Rohr, B.A., et al. (2019). A rigorous electrochemical ammonia synthesis protocol with quantitative isotope measurements. Nature *570*, 504–508. https://doi.org/10.1038/s41586-019-1260-x.

8. Singh, A.R., Rohr, B.A., Statt, M.J., Schwalbe, J.A., Cargnello, M., and Nørskov, J.K. (2019). Strategies toward Selective Electrochemical Ammonia Synthesis. ACS Catal. *9*, 8316–8324. https://doi.org/10.1021/acscatal.9b02245.

9. Hu, L., Khaniya, A., Wang, J., Chen, G., Kaden, W.E., and Feng, X. (2018). Ambient Electrochemical Ammonia Synthesis with High Selectivity on Fe/Fe Oxide Catalyst. ACS Catal. *8*, 9312–9319. https://doi.org/10.1021/acscatal.8b02585.

10. Li, K., Andersen, S.Z., Statt, M.J., Saccoccio, M., Bukas, V.J., Krempl, K., Sa, R., Chakraborty, D., Kibsgaard, J., Vesborg, P.C.K., et al. (2021). Enhancement of Lithium-Mediated Ammonia Synthesis by Addition of Oxygen.

11. Lazouski, N., Chung, M., Williams, K., Gala, M.L., and Manthiram, K. (2020). Non-aqueous gas diffusion electrodes for rapid ammonia synthesis from nitrogen and water-splitting-derived hydrogen. Nat. Catal. *3*, 463–469. https://doi.org/10.1038/s41929-020-0455-8.

12. Lazouski, N., Schiffer, Z.J., Williams, K., and Manthiram, K. (2019). Understanding Continuous Lithium-Mediated Electrochemical Nitrogen Reduction. Joule *3*, 1127–1139. https://doi.org/10.1016/j.joule.2019.02.003.

13. Suryanto, B.H.R., Matuszek, K., Choi, J., Hodgetts, R.Y., Du, H.-L., Bakker, J.M., Kang, C.S.M., Cherepanov, P.V., Simonov, A.N., and MacFarlane, D.R. (2021). Nitrogen reduction to ammonia at high efficiency and rates based on a phosphonium proton shuttle. Science *372*, 1187–1191. https://doi.org/10.1126/science.abg2371.

14. MacFarlane, D.R., Cherepanov, P.V., Choi, J., Suryanto, B.H., Hodgetts, R.Y., Bakker, J.M., Ferrero Vallana, F.M., and Simonov, A.N. (2020). A Roadmap to the Ammonia Economy. Joule *4*, 1186–1205. https://doi.org/10.1016/j.joule.2020.04.004.

15. Krishnamurthy, D., Lazouski, N., Gala, M.L., Manthiram, K., and Viswanathan, V. (2021). Closed-Loop Electrolyte Design for Lithium-Mediated Ammonia Synthesis. ACS Cent. Sci. *7*, 2073–2082. https://doi.org/10.1021/acscentsci.1c01151.

16. Du, H.-L., Chatti, M., Hodgetts, R.Y., Cherepanov, P.V., Nguyen, C.K., Matuszek, K., MacFarlane, D.R., and Simonov, A.N. (2022). Electroreduction of nitrogen with almost 100% current-to-ammonia efficiency. Nature *609*, 722–727. https://doi.org/10.1038/s41586-022-05108-y.

17. Montoya, J.H., Tsai, C., Vojvodic, A., and Nørskov, J.K. (2015). The Challenge of Electrochemical Ammonia Synthesis: A New Perspective on the Role of Nitrogen Scaling Relations. ChemSusChem *8*, 2180–2186. https://doi.org/10.1002/cssc.201500322.

18. Duan, G.Y., Ren, Y., Tang, Y., Sun, Y.Z., Chen, Y.M., Wan, P.Y., and Yang, X.J. (2020). Improving the Reliability and Accuracy of Ammonia Quantification in Electro- and Photochemical Synthesis. ChemSusChem *13*, 88–96. https://doi.org/10.1002/cssc.201901623.

19. Kolen, M., Ripepi, D., Smith, W.A., Burdyny, T., and Mulder, F.M. (2022). Overcoming Nitrogen Reduction to Ammonia Detection Challenges: The Case for Leapfrogging to Gas Diffusion Electrode Platforms. ACS Catal. *12*, 5726–5735. https://doi.org/10.1021/acscatal.2c00888.

20. Zaffaroni, R., Ripepi, D., Middelkoop, J., and Mulder, F.M. (2020). Gas Chromatographic Method for *In Situ* Ammonia Quantification at Parts per Billion Levels. ACS Energy Lett. *5*, 3773–3777. https://doi.org/10.1021/acsenergylett.0c02219.

21. Greenlee, L.F., Renner, J.N., and Foster, S.L. (2018). The Use of Controls for Consistent and Accurate Measurements of Electrocatalytic Ammonia Synthesis from Dinitrogen. ACS Catal. *8*, 7820–7827. https://doi.org/10.1021/acscatal.8b02120.

22. van Langevelde, P.H., Katsounaros, I., and Koper, M.T. (2021). Electrocatalytic Nitrate Reduction for Sustainable Ammonia Production. Joule *5*, 290–294. https://doi.org/10.1016/j.joule.2020.12.025.

23. Duca, M., and Koper, M.T.M. (2012). Powering denitrification: the perspectives of electrocatalytic nitrate reduction. Energy Environ. Sci. *5*, 9726. https://doi.org/10.1039/c2ee23062c.

24. Chauhan, R., and Srivastava, V.C. (2021). Superior reduction of nitrate with simultaneous oxidation of intermediates and enhanced nitrogen gas selectivity via novel electrochemical treatment. Process Saf. Environ. Protect. *147*, 245–258. https://doi.org/10.1016/j.psep.2020.09.026.

25. Song, Q., Li, M., Wang, L., Ma, X., Liu, F., and Liu, X. (2019). Mechanism and optimization of electrochemical system for simultaneous removal of nitrate and ammonia. J. Hazard Mater. *363*, 119–126. https://doi.org/10.1016/j.jhazmat.2018.09.046.

26. Wang, Y., Xu, A., Wang, Z., Huang, L., Li, J., Li, F., Wicks, J., Luo, M., Nam, D.-H., Tan, C.-S., et al. (2020). Enhanced Nitrate-to-Ammonia Activity on Copper–Nickel Alloys via Tuning of Intermediate Adsorption. J. Am. Chem. Soc. *142*, 5702–5708. https://doi.org/10.1021/jacs.9b13347.

27. Wu, Z.-Y., Karamad, M., Yong, X., Huang, Q., Cullen, D.A., Zhu, P., Xia, C., Xiao, Q., Shakouri, M., Chen, F.-Y., et al. (2021). Electrochemical ammonia synthesis via nitrate reduction on Fe single atom catalyst. Nat. Commun. *12*, 2870. https://doi.org/10.1038/s41467-021-23115-x.

28. Chen, G.-F., Yuan, Y., Jiang, H., Ren, S.-Y., Ding, L.-X., Ma, L., Wu, T., Lu, J., and Wang, H. (2020). Electrochemical reduction of nitrate to ammonia via direct eight-electron transfer using a copper–molecular solid catalyst. Nat. Energy *5*, 605–613. https://doi.org/10.1038/s41560-020-0654-1.

29. Carvalho, O.Q., Marks, R., Nguyen, H.K.K., Vitale-Sullivan, M.E., Martinez, S.C., Árnadóttir, L., and Stoerzinger, K.A. (2022). Role of Electronic Structure on Nitrate Reduction to Ammonium: A Periodic Journey. J. Am. Chem. Soc. *144*, 14809–14818. https://doi.org/10.1021/jacs.2c05673.

30. Chen, F.-Y., Wu, Z.-Y., Gupta, S., Rivera, D.J., Lambeets, S.V., Pecaut, S., Kim, J.Y.T., Zhu, P., Finfrock, Y.Z., Meira, D.M., et al. (2022). Efficient conversion of low-concentration nitrate sources into ammonia on a Ru-dispersed Cu nanowire electrocatalyst. Nat. Nanotechnol. *17*, 759–767. https://doi.org/10.1038/s41565-022-01121-4.

31. Han, S., Li, H., Li, T., Chen, F., Yang, R., Yu, Y., and Zhang, B. (2023). Ultralow overpotential nitrate reduction to ammonia via a three-step relay mechanism. Nat. Catal. *6*, 402–414. https://doi.org/10.1038/s41929-023-00951-2.

32. He, W., Zhang, J., Dieckhöfer, S., Varhade, S., Brix, A.C., Lielpetere, A., Seisel, S., Junqueira, J.R.C., and Schuhmann, W. (2022). Splicing the active phases of copper/cobalt-based catalysts achieves high-rate tandem electroreduction of nitrate to ammonia. Nat. Commun. *13*, 1129. https://doi.org/10.1038/s41467-022-28728-4.

33. Jeon, T.H., Wu, Z.-Y., Chen, F.-Y., Choi, W., Alvarez, P.J.J., and Wang, H. (2022). Cobalt–Copper Nanoparticles on Three-Dimensional Substrate for Efficient Ammonia Synthesis via Electrocatalytic Nitrate Reduction. J. Phys. Chem. C *126*, 6982–6989. https://doi.org/10.1021/acs.jpcc.1c10781.

34. Pérez-Gallent, E., Figueiredo, M.C., Katsounaros, I., and Koper, M.T. (2017). Electrocatalytic reduction of Nitrate on Copper single crystals in acidic and alkaline solutions. Electrochim. Acta *227*, 77–84. https://doi.org/10.1016/j.electacta.2016.12.147.

35. Wang, Y., Li, H., Zhou, W., Zhang, X., Zhang, B., and Yu, Y. (2022). Structurally Disordered RuO_2 Nanosheets with Rich Oxygen Vacancies for Enhanced Nitrate Electroreduction to Ammonia. Angew. Chem. Int. Ed. *61*, e202202604. https://doi.org/10.1002/anie.202202604.

36. John, J., MacFarlane, D.R., and Simonov, A.N. (2023). The why and how of NOx electroreduction to ammonia. Nat. Catal. *6*, 1125–1130. https://doi.org/10.1038/s41929-023-01060-w.

37. Li, P., Li, R., Liu, Y., Xie, M., Jin, Z., and Yu, G. (2023). Pulsed Nitrate-to-Ammonia Electroreduction Facilitated by Tandem Catalysis of Nitrite Intermediates. J. Am. Chem. Soc. *145*, 6471–6479. https://doi.org/10.1021/jacs.3c00334.

38. Bunea, S., Clemens, K., and Urakawa, A. (2022). Electrified Conversion of Contaminated Water to Value: Selective Conversion of Aqueous Nitrate to Ammonia in a Polymer Electrolyte Membrane Cell. ChemSusChem *15*, e202102180. https://doi.org/10.1002/cssc.202102180.

39. Ahsan, M., Hossain, M.M., Almahri, A., Rahman, M.M., and Hasnat, M.A. (2022). Optimisation and Stability of Rh Particles on Noble Metal Films Immobilised on H^+ Conducting Solid Polymer Electrolyte in Attaining Efficient Nitrate Removal. Chem. Asian J. *17*, e202200150. https://doi.org/10.1002/asia.202200150.

40. Li, S., Han, D., Jiang, G., Han, Z., Lu, H., Gao, J., Wang, X., Wang, Y., Geng, C., Weng, Z., and Yang, Q.H. (2023). Proton Exchange Membrane Electrode Assembly for Ammonia Electrosynthesis from Nitrate. ACS Appl. Energy Mater. *6*, 5067–5073. https://doi.org/10.1021/acsaem.3c00709.

41. Kibria, M.G., Edwards, J.P., Gabardo, C.M., Dinh, C.T., Seifitokaldani, A., Sinton, D., and Sargent, E.H. (2019). Electrochemical CO_2 Reduction into Chemical Feedstocks: From Mechanistic Electrocatalysis Models to System Design. Adv. Mater. *31*, 1807166. https://doi.org/10.1002/adma.201807166.

42. Burdyny, T., and Smith, W.A. (2019). CO_2 reduction on gas-diffusion electrodes and why catalytic performance must be assessed at commercially-relevant conditions. Energy Environ. Sci. *12*, 1442–1453. https://doi.org/10.1039/C8EE03134G.

43. Iglesias Van Montfort, H.-P., Subramanian, S., Irtem, E., Sassenburg, M., Li, M., Kok, J., Middelkoop, J., and Burdyny, T. (2023). An Advanced Guide to Assembly and Operation of CO_2 Electrolyzers. ACS Energy Lett. *8*, 4156–4161. https://doi.org/10.1021/acsenergylett.3c01561.

44. Lees, E.W., Goldman, M., Fink, A.G., Dvorak, D.J., Salvatore, D.A., Zhang, Z., Loo, N.W.X., and Berlinguette, C.P. (2020). Electrodes Designed for Converting Bicarbonate into CO. ACS Energy Lett. *5*, 2165–2173. https://doi.org/10.1021/acsenergylett.0c00898.

45. Ren, Z., Shi, K., and Feng, X. (2023). Elucidating the Intrinsic Activity and Selectivity of Cu for Nitrate Electroreduction. ACS Energy Lett. *8*, 3658–3665. https://doi.org/10.1021/acsenergylett.3c01226.

46. Yang, K., Kas, R., Smith, W.A., and Burdyny, T. (2021). Role of the Carbon-Based Gas Diffusion Layer on Flooding in a Gas Diffusion Electrode Cell for Electrochemical CO_2 Reduction. ACS Energy Lett. *6*, 33–40. https://doi.org/10.1021/acsenergylett.0c02184.